Hybrid magnetohydrodynamic-kinetic electron closure methods and shear Alfvén waves in nonuniform plasmas

P. A. Damiano[a] and A. N. Wright
Mathematical Institute, University of St. Andrews, St. Andrews, Fife KY16 9SS, United Kingdom

R. D. Sydora[b]
Institut fuer Theoretische Physik I, Heinrich-Heine-Universitaet, Duesseldorf, Germany

J. C. Samson
Department of Physics, University of Alberta, Edmonton, Alberta, Canada, T6G 2J1

(Received 20 August 2004; accepted 20 December 2004; published online 17 March 2005)

Two hybrid magnetohydrodynamic-kinetic electron models of shear Alfvén waves with different closure schemes involving the assumption of quasineutrality are compared. One method assumes quasineutrality directly while the other allows for a nonzero $\nabla\cdot\vec{j}$ that produces a "correcting" electric field. The interpretation of the different closure schemes is discussed and the two methods are shown to yield consistent results for both the cases of a constant and variable density along the field line. In the variable density case the hybrid system with and without a shear Alfvén wave perturbation is also contrasted. In the latter case, static parallel electric fields that increased with the plasma temperature were generated to support the density gradients. When the system was perturbed, a time dependent parallel electric field contribution oscillated around the static field structure needed to support the profile. Landau damping effects were also investigated and the energy invariant for the systems derived. © *2005 American Institute of Physics*.
[DOI: 10.1063/1.1862627]

I. INTRODUCTION

Shear Alfvén wave pulses or standing waves (called geomagnetic field line resonances) on closed magnetic field lines are common occurrences in the earth's magnetosphere. To lowest order, the structure of their currents can be seen as ion polarization currents perpendicular to the ambient magnetic field closed by electron currents parallel to the field line, which together maintain quasineutrality. Traditional magnetohydrodynamic (MHD) models (in the limit of $m_e \rightarrow 0$, $E_z \rightarrow 0$) have had much success in the study of the formation and evolution of such systems, but in order to make the link to auroral arc formation, information on the parallel electric field is needed to study the electron acceleration process. Incorporating electron mass via the inclusion of the generalized Ohm's law allows for the study of the parallel electric field in the MHD description,[1,2] but these studies neglect potentially important effects such as the mirror force contributions[3,4] and do not elucidate anything about the structure of the electron distribution functions.[2] Therefore models incorporating a kinetic electron description and wave-particle interactions are required.

Models using particles or direct Vlasov solution for either the ions or electrons while the other species is described by fluid equations are generally known as hybrid models. Such simulation models with particle ions and fluid electrons have been extensively used to investigate nonlinear processes in laboratory and space plasmas. Some of the early hybrid simulation models were applied to the study of laboratory pinch experiments[5–8] and the structure of the magnetospheric bow shock.[9] Subsequent developments have mainly been in multidimensional simulation models[10] with application to collisionless shocks,[11,12] magnetic reconnection,[13] and ion beam instabilities.[14] There have been relatively few investigations using fluid ion and particle/kinetic electron hybrid models[15] but as alluded to above, this type of hybrid approach is needed for the study of shear Alfvén waves associated with auroral arc formation. In recent years, the focus has been primarily on Alfvén wave pulses using test-particle simulations[16–19] and more self- consistent numerical hybrid approaches representing the electrons in a Vlasov type formulation[20] or combining MHD with a system of kinetic electrons in a particle-in-cell (PIC) type formulation.[21] To a lesser extent, standing shear Alfvén waves have also been studied in the context of a hybrid MHD-kinetic electron model[22] (which is a variation of the approach used in Ref. 21 as well as more analytical studies which combine MHD with a Vlasov equation for the electrons,[3,23,24] some of which incorporate mirror force effects.[3,23]

In this paper we consider standing shear Alfven wave dynamics within a hybrid MHD-kinetic framework (fluid ion, kinetic electron) and compare two different closure schemes, with and without the assumption of quasineutrality. Typical scale lengths in auroral plasmas are 1–100 km much greater than the electron gyroradius and Debye length, and with frequencies much below the plasma frequency. Therefore, we use a cold ion fluid model with electron dynamics treated in the guiding center approximation. One approach (used in Ref. 21 for the study of electron acceleration by shear Alfvén wave breaking) assumes quasineutrality di-

[a]Electronic mail: pdamiano@mcs.st-and.ac.uk
[b]Also at Department of Physics, University of Alberta.

rectly ($\nabla\cdot\vec{j}\approx 0$), and will be termed zeroth order. A first order approach was used by Ref. 22 and does not directly assume quasineutrality but allows for a nonzero $\nabla\cdot\vec{j}$ which produces a corresponding perpendicular electric field contribution. This in-turn affects the parallel electric field via the generalized Ohm's law. For limits where the plasma wants to maintain quasineutrality, it can be viewed as a correcting electric field. The zeroth order model is one-dimensional (1D) field aligned while the first order model is 2D. However in the 2D case, the radial density (x) is assumed constant and the shear Alfvén wave perturbation periodic, making it straightforward to draw comparisons between the two models. In addition to this comparison, the work extends the consideration of standing waves begun in Ref. 22 to the case of nonuniform plasmas.

The paper has four main sections. In the first section, the MHD and two hybrid approaches are summarized. In the second section; the MHD and hybrid approaches and then the two hybrid approaches themselves are contrasted for a constant density system. The third section considers the case of inhomogeneity with a field aligned density gradient in both the static limit and for the system with a shear Alfvén wave perturbation, where Landau damping effects will be examined. The fourth section contains a concluding summary and the energy invariant for both hybrid models is derived in the Appendix.

II. DESCRIPTION OF MODELS

A. Cold plasma MHD model

In the MHD limit ($\omega_{MHD}\ll\omega_{pe}, L\gg\lambda_D, r_{g_i}$), the plasma is quasineutral ($\nabla\cdot\vec{j}=0$, $n_i=n_e$) on length scales $L\gg\lambda_D$, where L is the characteristic length scale of the system, λ_D is the Debye length, and r_{g_i} is the typical ion gyroradius. The acceleration of electrons along the field line is proportional to $-eE_z/m_e$ and so $m_e\to 0$ and $E_z\to 0$ at the same rate in the MHD picture. The response of the electrons is instantaneous.

A 1D plasma model along a magnetic field line pointing in the z direction is considered and assuming $\partial/\partial y=0$, a simple cold plasma MHD model for a shear Alfvén wave system is given by

$$\frac{\partial\alpha}{\partial t}=-\mu_o V_A^2\frac{\partial j_z}{\partial z}, \tag{1}$$

$$\frac{\partial j_z}{\partial t}=-\frac{1}{\mu_o}\frac{\partial\alpha}{\partial z}, \tag{2}$$

where $\alpha=\partial E_x/\partial x$ and $V_A=B_o/\sqrt{\mu_o\rho}$ is the Alfvén wave speed. The first equation can be derived from the single fluid momentum equation and the ideal MHD approximation (or the definition of the polarization current) along with quasineutrality ($\partial j_z/\partial z=-\partial j_x/\partial x$) and represents the polarization current due to ions. Of course, a finite δn_e is needed to balance α. However, this is on MHD time scales and the quasineutrality condition applies on the time scale of the plasma frequency. Therefore it is not contradictory to use $\nabla\cdot\vec{j}=0$ on the right-hand side (RHS) of Eq. (1). The derivation assumes that there is no perpendicular gradient in V_A (or ρ), otherwise an extra term arises and the system is more complicated to deal with. The second equation is derived from Ampère's ($\mu_o j_z=\partial b_y/\partial x$) and Faraday's laws ($\partial b_y/\partial t=-\partial E_x/\partial z$) and incorporates the massless electrons response to maintain quasineutrality.

B. Zeroth order hybrid approach: Direct assumption of quasineutrality

For the zeroth order hybrid model developed in Ref. 21, the same basic assumptions (except $m_e=0$) used in the MHD model hold as well. The initial equation representing ion perpendicular polarization current is the same as in the preceding section (including built in quasineutrality condition). Finite but small electron mass yields a finite ω_{pe}, however, $\omega_{MHD}\ll\omega_{pe}$ still holds and one can use $\nabla\cdot\vec{j}=0$.

With $m_e\neq 0$ now, Eq. (2) is replaced by an actual system of electrons and the generalized Ohm's law is used for computing the parallel electric field. Since the typical electron gyroradius is so much smaller than typical MHD scale lengths, the guiding center equations can be used for the parallel electron dynamics and the model equations can be expressed as

$$\frac{\partial}{\partial t}\left(\frac{\partial E_x}{\partial x}\right)=\frac{\partial\alpha}{\partial t}=-\mu_o V_A^2\frac{\partial j_e}{\partial z}, \tag{3}$$

$$m_e\frac{dv_z}{dt}=-eE_z, \tag{4}$$

$$\frac{dr_z}{dt}=v_z, \tag{5}$$

$$E_z=-\frac{1}{1+\lambda_e^2k_x^2}\left(\lambda_e^2\frac{\partial\alpha}{\partial z}+\frac{m_e}{ne}\frac{\partial D_e}{\partial z}\right), \tag{6}$$

where Eqs. (4) and (5) are the guiding center equations and Eq. (6) is the generalized Ohm's law. In this version, Faraday's law and Ampère's law have been used to replace the term with the partial time derivative of current density and the equation is a 1D analog of the parallel electric field equation used in Refs. 21 and 22. The quantity $j_e=-e\Sigma_i v_{z_i}S(r_{z_i},z)$ is the parallel current computed from the electrons, $D_e=\Sigma_i v_{z_i}^2S(r_{z_i},z)$ (using the notation of Ref. 21) is the second moment of the electron distribution function, and $S(r_{z_i},z)$ is the particle shape function (see Ref. 25) which is also related to the interpolation of the moments to the grid cells. The electron inertial length $\lambda_e=\sqrt{m_e/\mu_o ne^2}$ defines the fundamental length scale on which electron mass effects become important (usually below about $10\lambda_e$) and evolves as a function of the electron number density $n_e=\Sigma_i S(r_{z_i},z)$ to be consistent with the assumption of quasineutrality ($n=n_i=n_e$). The Alfvén speed V_A similarly evolves (via $\rho=nm_i$).

C. First order hybrid approach

In the first order approach we do not fix the value of $\nabla\cdot\vec{j}$, but allow for a first order correction via the perpendicular electric field contribution. If the plasma wants to be quasineutral, but the parallel electron current differs from the

divergence free MHD solution, a correcting field is produced to compensate. Therefore quasineutrality is a result rather than an initial assumption we impose on the model. It can be viewed as a numerical analog to a physical plasma oscillation produced in a bid to maintain quasineutrality. In Ref. 22, this correcting electric field was introduced as a separate step, but will be reformulated here in a more self-consistent way as an extension of the zeroth order assumption of quasineutrality as defined previously.

First of all, as in Ref. 22 the model consists of the cold plasma MHD equations given by (for $\partial/\partial y=0$)

$$\frac{\partial u_x}{\partial t}=\frac{B_o}{\mu_o\rho_o}\left(\frac{\partial b_x}{\partial z}-\frac{\partial b_z}{\partial x}\right), \tag{7}$$

$$\frac{\partial u_y}{\partial t}=\frac{B_o}{\mu_o\rho_o}\frac{\partial b_y}{\partial z},$$

$$\frac{\partial b_x}{\partial t}=\frac{\partial E_y}{\partial z},$$

$$\frac{\partial b_y}{\partial t}=\frac{\partial E_z}{\partial x}-\frac{\partial E_x}{\partial z},$$

$$\frac{\partial b_z}{\partial t}=-\frac{\partial E_y}{\partial x},$$

coupled to a system of kinetic electrons which evolve according to the guiding center equations [Eqs. (4) and (5)] and the perpendicular electric field comes from the ideal MHD approximation $\vec{E}_\perp=\vec{u}\times\vec{B}$. In Eq. (7) all variables are a function of x and z and a variable dependence of $\sin(k_y y)$ for u_x has been assumed and factored through. The system is closed via the expression for the parallel electric field (where the difference from Ref. 22 emerges).

Starting with the 2D analog of generalized Ohm's law, given in Eq. (6), and with the additional assumption of $k_x^2 \ll \lambda_e^{-2}$, the equation for the parallel electric field reduces to

$$E_z=-\left(\lambda_e^2\frac{\partial\alpha}{\partial z}+\frac{m_e}{ne}\frac{\partial D_e}{\partial z}\right). \tag{8}$$

Now considering the full Ampère's law,

$$\nabla\times\vec{B}=\mu_o\vec{j}+\mu_o\epsilon_o\frac{\partial\vec{E}}{\partial t}, \tag{9}$$

and taking the divergence of both sides we are left with

$$\epsilon_o\frac{\partial(\nabla\cdot\vec{E})}{\partial t}=-\nabla\cdot\vec{j}, \tag{10}$$

which is the same expression as derived in Ref. 22 using Poisson's equation and the continuity equations for the electrons and ions. Since $E_z \ll E_\perp$ and $k_y=0$, Eq. (10) can be rewritten as

$$\epsilon_o\frac{\partial\alpha}{\partial t}=-\nabla\cdot\vec{j}=-\left(\frac{\partial j_x}{\partial x}+\frac{\partial j_z}{\partial z}\right). \tag{11}$$

Now, due to the low frequency nature of MHD it is customary to neglect the displacement current yielding $\nabla\cdot\vec{j}_{MHD}\approx 0$ which is one form of the statement of quasineutrality. However, imagine that at a given time t the electrons are in a position so that the electron current is not in exact agreement with the MHD current. Therefore, we can let $\vec{j}=\vec{j}_{MHD}+\delta\vec{j}$ and $\nabla\cdot\vec{J}>\nabla\cdot\vec{J}_{MHD}$ which, via Eq. (11), yields an additional contribution to E_x. Therefore, the total value of α is

$$\alpha=\alpha_{MHD}+\delta\alpha=\alpha_{MHD}+\alpha_c, \tag{12}$$

where $\alpha_{MHD}=-\partial/\partial x(\vec{u}\times B_o)=-(\partial u_y/\partial x)B_o$ and α_c has been introduced for consistency of notation with Ref. 22. With this, Eq. (11) becomes

$$\epsilon_o\frac{\partial}{\partial t}(\alpha_{MHD}+\alpha_c)=-(\nabla\cdot\vec{j}_{MHD}+\nabla\cdot\delta\vec{j}), \tag{13}$$

and since $\partial\alpha_{MHD}/\partial t=\nabla\cdot\vec{j}_{MHD}\approx 0$ this can be reduced to

$$\epsilon_o\frac{\partial\alpha_c}{\partial t}=-\nabla\cdot\delta\vec{j}=-\nabla\cdot\vec{j}. \tag{14}$$

Using Eq. (12), the expression for the parallel electric field becomes

$$E_z=-\left(\lambda_e^2\frac{\partial\alpha_{MHD}}{\partial z}+\frac{m_e}{ne}\frac{\partial D_e}{\partial z}+\lambda_e^2\frac{\partial\alpha_c}{\partial z}\right) \tag{15}$$

or using Eq. (11) it can also be expressed as

$$E_z=-\left(\lambda_e^2\frac{\partial\alpha_{MHD}}{\partial z}+\frac{m_e}{ne}\frac{\partial D_e}{\partial z}-\frac{\lambda_e^2}{\epsilon_o}\frac{\partial}{\partial z}\int_0^t dt\,\nabla\cdot\vec{j}\right), \tag{16}$$

where the parallel current density used in the calculation of $\nabla\cdot\vec{j}$ is computed directly from the electrons which are again advanced using the guiding center equations. The evaluation of the integral over time is done using a simple Euler scheme. At a specific time t, the integral is advanced in a predictor step with the value of $\nabla\cdot\vec{j}$ determined from the predicted fields and then the final value of the integral is computed using the average of the divergence in current density computed using the predicted and corrected fields. As indicated previously, the approach is a little different than that used in Ref. 22, but yields consistent results. Also as in Ref. 22, the electron inertial length λ_e is fixed at its equilibrium value.

In summary, Eqs. (4), (5), (7), and (16) along with the ideal MHD approximation for the perpendicular electric field constitute the 2D first order hybrid model. For simplicity of notation any future reference to the 2D hybrid model will have the first order nature and any reference to the 1D hybrid model will have the zeroth order nature.

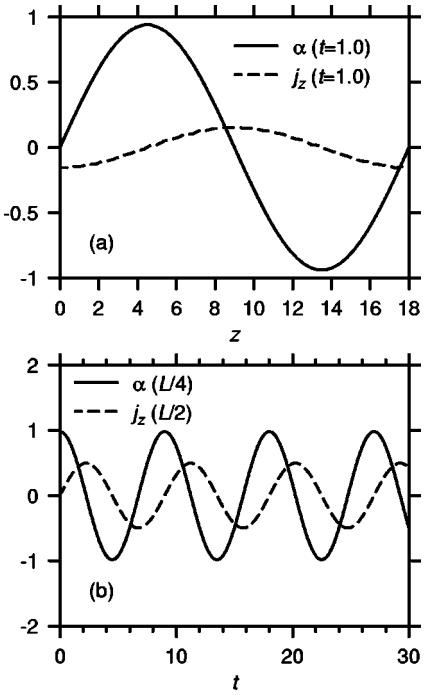

FIG. 1. Solution of the 1D MHD equations excluding electron inertial effects. (a) Relative profiles of α and j_z as a function of z at $t=0.5$. (b) Evolution of the amplitude of both α and j_z as a function of time.

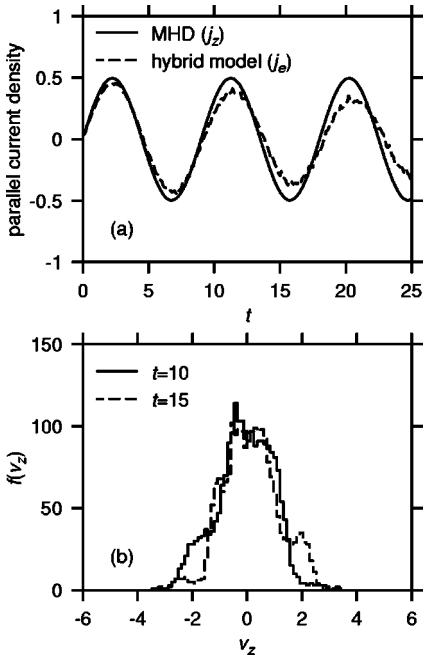

FIG. 2. (a) Comparison of the evolution of j_z (at $L/2$) in the MHD and 1D hybrid model for $v_{th}=1.41$ illustrating Landau damping effects in the latter case. (b) Evolution of the local distribution function between $z=9.0$ and $z=9.5$ for the hybrid model illustrating the accelerated electron populations at $v_{ph}=\omega/k_z=\pm 2$ (v_z is normalized by V_A). The perturbation of the accelerated population cycles from side to side as current changes sign.

III. SIMULATIONS WITH CONSTANT DENSITY

A. Method outline

As done in Ref. 22, the first order differential equations ($dy/dt=F$) are finite differenced in time using the predictor-corrector approach

$$y_p^{t+\Delta t} = y^{t-\Delta t} + 2\Delta t F(y^t), \tag{17}$$

$$y^{t+\Delta t} = y^t + \frac{\Delta t}{2}[F(y^t) + F(y_p^{t+\Delta t})], \tag{18}$$

where the subscript p denotes the predictor step and the spatial derivatives are calculated using the same four point finite difference scheme as used in Ref. 22. The magnetic field is normalized by the ambient magnetic field $B_o=10$ nT, length by an earth radius ($L_N=R_E$), density by $\rho_N=0.1m_p$ cm^{-3}, and velocity by $V_N=\sqrt{B_o^2/(\mu_o\rho_N)}$. With these definitions, time is normalized by $t_N=L_N/V_A$, electric field by $E_N=V_N B_o$, and the current density by $j_N=B_o/(\mu_o L_N)$. All plots are done in terms of nondimensional variables.

B. Comparison of MHD and 1D hybrid models

The system is perturbed by a sinusoidal α profile at $t=0$ given by

$$\alpha_o = A\sin\left(\frac{2\pi z}{L}\right), \tag{19}$$

where $A=1.0$ and $L=18$ is the length of the simulation box in nondimensional units. Most of the parameters were chosen to be consistent with those used in Ref. 22 and periodic boundary conditions were assumed. For the 2D hybrid model, periodic boundary conditions were also used in z and open boundary conditions ($\partial/\partial x=0$) in x. In nondimensional units, the background magnetic field is 1, $V_A=2$, and $\rho_o=0.25$.

Figure 1 illustrates the relative evolution of α and j_z as a function of time for the MHD system. This result is contrasted in Fig. 2 where the MHD and 1D hybrid models (using $v_{th}=1.41$) solutions are plotted simultaneously. Landau damping effects (as discussed in Ref. 22) are clearly evident. In both simulations 50 grid points and a time step of 0.0014 in nondimensional units were used. The hybrid simulation was done using 80 000 simulation electrons.

The energy invariant of the 1D hybrid system (see the Appendix) is given simply in nondimensional form by

$$T_{E_{1D}} = -\int_0^t \int_0^{L_z} (E_Z j_e) dz dt + \frac{1}{2} C_{e1} \sum_i v_i^2, \tag{20}$$

where the first term is the Poynting flux energy entering the 1D elemental flux tube from perpendicular to the field line, the second term is the kinetic energy of the electron motion along the field line, and C_{e1} is a dimensionless constant (see the Appendix). The result for the $v_{th}=1.41$ case is illustrated in Fig. 3(a) showing that energy is conserved between the electrons and fluid during the Landau damping process. Figure 3(b) shows the relative numerical error in the energy as a function of time which is well below 0.01% for the length of the run. High frequency oscillations develop as the grid scale noise due to the particle interpolation scheme builds up and the overall error decreases with time as the wave amplitude is reduced due to Landau damping. The effects of the grid scale noise over the longer term are worse for larger grid

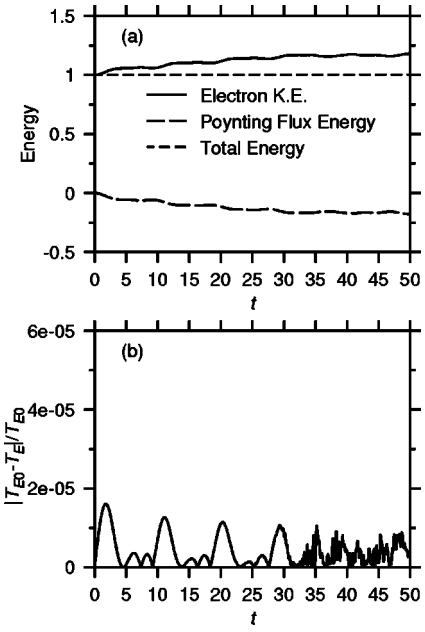

FIG. 3. (a) Total and component energies vs time for the 1D hybrid models with $v_{th}=1.41$. (b) Relative error in total energy T_E as a function of time.

spacings as the fluctuations represent a significant fraction of the actual wavelength of the shear Alfvén wave. Therefore, finer grid spacings achieve better results for longer runs but require significantly larger numbers of particles to achieve similar results with regards to the resolution of the parallel electric field. For the results here, we have chosen the grid scale and particle number to obtain the best results for the first 3–4 Alfvén periods which is sufficient to demonstrate the operation of the code without needing too much computational time.

C. Comparison of hybrid models

The hybrid models are contrasted by selecting an initial u_y profile periodic in x as well as z and using a profile of $\partial E_x/\partial x$ for a slice along a certain value of x for the 1D model. The initial profile chosen for the 2D model was

$$u_{y_0} = 0.05 \sin\left(\frac{2\pi x}{0.2}\right) e^{-(x-0.5)^8/0.0001} \sin\left(\frac{2\pi z}{L}\right). \tag{21}$$

The exponential cutoff in the x direction was used to minimize any edge effects from the boundaries [where open boundary conditions are assumed $(\partial/\partial x=0)$]. The dependence as a function of x is illustrated in Fig. 4. In terms of the 1D model, we take the initial parameters so that it represents a line along z at $x=0.5$. Therefore the initial profile for α is given by

$$\alpha_0 = \frac{\partial E_x}{\partial x} = -\frac{\partial u_{y_0}}{\partial x} = -0.05\frac{2\pi}{0.2}\cos\left(\frac{2\pi 0.5}{0.2}\right)\sin\left(\frac{2\pi z}{L}\right), \tag{22}$$

where $B_o=1$ in nondimensional units and although not stated explicitly in the equation, this corresponds to a value for k_x of $2\pi/0.2$.

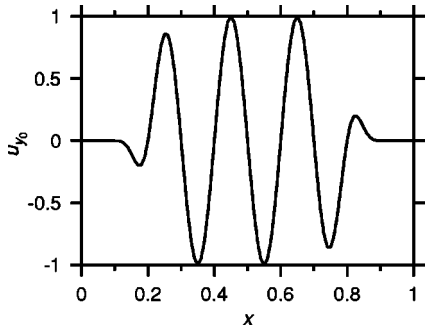

FIG. 4. Variation with respect to x of initial u_y perturbation used in the 2D hybrid model.

Figure 5 illustrates the amplitude of the electron current density as a function of time for both the 1D and 2D models with $v_{th}=0.71$. The point of interest is the divergence between the 1D model results with and without the pressure term. As indicated in Ref. 22, for the 2D model results, the pressure term had insignificant contribution. The explanation for this difference in the importance of this term in the context of the 2D model will be highlighted in the following section. For the 2D model simulations presented in this section, 200 grid points were chosen in the x direction and 25 were chosen in the z direction, 10^6 simulation electrons were used ($n_{p_x}=1000, n_{p_z}=1000$), and the time step was 0.000 71. The 2D MHD results were obtained using the 2D hybrid model with the kinetic electron effects turned off [reducing the model to Eqs. (7) and (16) without the last two terms].

The fact that quasineutrality is maintained both in the 1D and 2D models is illustrated in Fig. 6 with the plotting of the divergence of the current density along with the component terms. In the 2D model, the divergence is computed directly from j_x and j_z while in the 1D model j_x is first calculated from α using

$$\frac{\partial j_x}{\partial x} = \frac{\rho}{B_o^2}\frac{\partial}{\partial t}\left(\frac{\partial E_x}{\partial x}\right) = \frac{\rho}{B_o^2}\frac{\partial \alpha}{\partial t}, \tag{23}$$

which has been derived from the single fluid momentum equation. The time derivative is calculated simply using the present and previous time step values of α. Although not the most accurate method, it serves to illustrate that quasineutral-

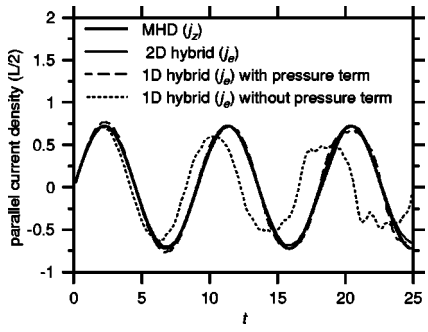

FIG. 5. Parallel current density (at $z=L/2$) for the 2D MHD model, the 2D hybrid model (excluding pressure term in E_z), and the 1D hybrid models with and without pressure term for $v_{th}=0.71$. The 2D model results were taken at the grid point closest to $x=0.5$.

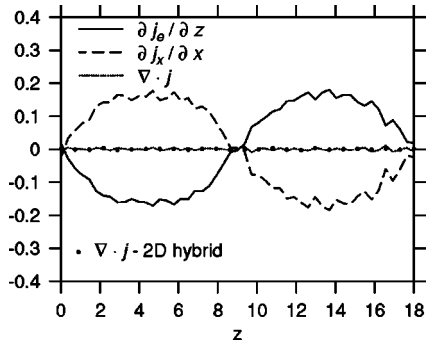

FIG. 6. Divergence of the current density and component quantities for the 1D hybrid model at $t=8$ and with $v_{th}=0.71$. The 2D hybrid model values, for the slice in z closest to $x=0.5$, are plotted as points.

ity is properly maintained. This is as would be expected given the initial assumptions for the 1D model. The points plotted for the 2D model serve to illustrate that even without the direct assumption of quasineutrality, the use of the correction field method served to maintain quasineutrality to good order. It should be noted that the results plotted here are for close to maximum current density values. As these values decrease, grid scale noise increases fluctuations in the divergence calculation, but this can be lessened with increased resolution.

The total energy invariant for the 2D hybrid model is given by (see the Appendix)

$$T_{E_{2D}} = T_{u_y} + T_{b_y} + T_e = \int_A dxdz \frac{\rho_o u_y^2}{2} + \int_A dxdz \frac{b_y^2}{2} + \frac{1}{2} C_{e2} \sum_i v_i^2 \tag{24}$$

and is displayed in Fig. 7 along with the individual terms in Eq. (24). In this case, the error in energy as a function of time increased almost linearly to a value of about 0.4% at $t=50$.

D. Interpretation

In order to elucidate the reason as to why the pressure term in the generalized Ohm's law is negligible for the 2D model we present two simulations with identical parameters except that in the first case the pressure term is included and

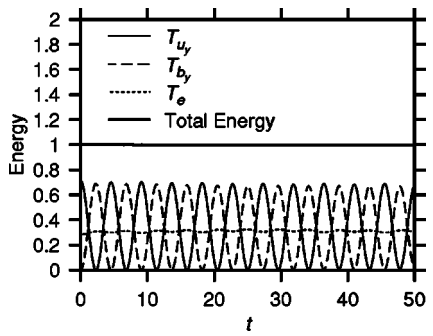

FIG. 7. Total and component energies vs time for the 2D hybrid model with $v_{th}=0.71$.

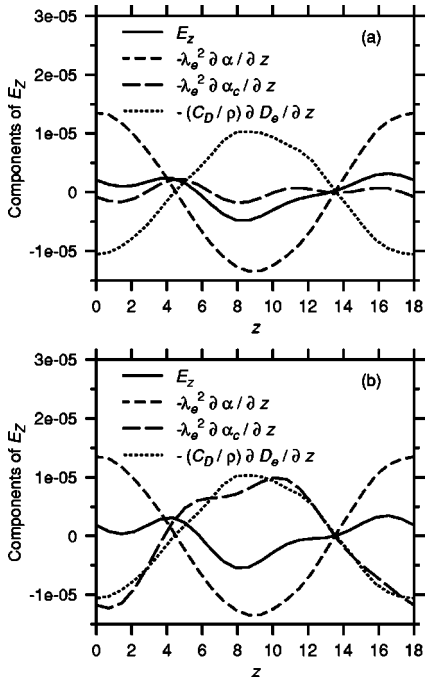

FIG. 8. Slices along z (closest to $x=0.5$) at $t=5$ of the terms in the equation for E_z for the 2D hybrid model including pressure (a) and excluding pressure (b). The curves for $\partial\alpha_c/\partial x$ and E_z have been smoothed using the same 2D spectral filter as outlined in Ref. 22.

in the second, it is excluded. For the following comparison, it is convenient to rewrite Eq. (15) in nondimensional form (as individual terms will be referenced in this notation) which is given by

$$E_z = -\left(\lambda_e^2 \frac{\partial \alpha}{\partial x} + C_D \frac{\partial D_e}{\partial z} + \lambda_e^2 \frac{\partial \alpha_c}{\partial z}\right), \tag{25}$$

where all variables are in nondimensional units and the normalization constant $C_D = m_e V_A/(eB_o L)$. For these simulations, the parameters are the same as for the 2D model in the preceding section except that $v_{th}=1.41$ was used to accentuate the pressure contribution. Figure 8 presents slices of the different terms in the equation for E_z at $t=5$ for both the case including (a) and excluding plasma pressure (b). This time was chosen as the pressure contribution is maximum when E_z and j_z are at a minimum. The curves for the α_c term and E_z have been smoothed using a postsimulation hyper-Gaussian spectral filter given by $e^{-(i/n)^{20}}$ where i is the spectral mode and n can be seen as a cutoff parameter. The filter was applied in both the x direction (with $n=80$) and in the z direction with $n=4$ to capture the first order Alfvén mode clearly, but cutout higher frequency noise. The same filter was used in Ref. 22 and more comment on its use can be found there.

It is evident that when the pressure term is included (a), the curve for the α_c term is small relative to the pressure term. However, when the pressure term is excluded (b) from the calculation for E_z, the α_c contribution rises to take the form of the missing pressure term. Although not shown here, similar runs were done for the higher temperature case $v_{th}=4.24$ and the same type of behavior was observed.

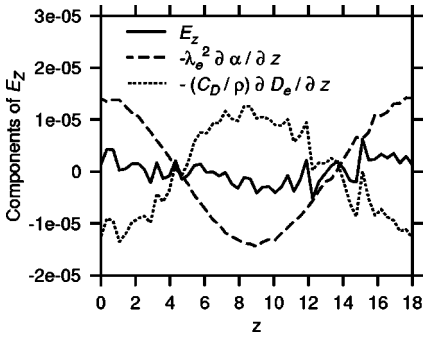

FIG. 9. Components of E_z from the 1D hybrid model for $v_{th}=1.41$ at $t=5$.

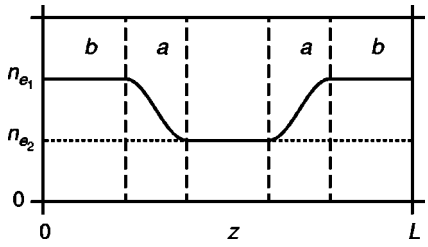

FIG. 10. Field aligned density profile in terms of the base parameters.

The explanation for this is that the bad guess for the parallel electric field leaves the distribution of electrons in a state that is not very quasineutral relative to the MHD fields. The resulting nonzero divergence leads to an electric field contribution which compensates for the lack of a pressure term, thus restoring quasineutrality. Since the system wants to be quasineutral, the algorithm allows for the creation of a compensating perpendicular electric field which more or less compensates for what the inclusion of a pressure term would have provided. This can possibly be viewed as a numerically created plasma oscillation, but since it is of much higher frequency than the Alfvén time scales that dictate the rest of the system, it does not affect the results in any significant way. This methodology would not distinguish between physical and numerical sources of quasineutrality violation and so caution must be used in interpreting the importance of the individual terms. As far as the algorithm is concerned, the generalized Ohm's law is simply an initial good guess to the parallel electric field.

Whereas this method can be viewed to oscillate around the proper solution, the direct assumption of quasineutrality can be viewed as specifying exactly what the solution should be on an instantaneous time scale. Therefore, all the information about the parallel electric field must be contained in the generalized Ohm's law to be transferred instantaneously. If a term is missing, then the physics associated with that term is lost.

Figure 9 illustrates the components of the parallel electric field from the 1D model when the pressure term has been included in the generalized Ohm's law. The fact that the two models give the same result under these conditions is emphasized here in comparison with Fig. 8 as the structure of the fields are basically the same. The 1D model results have not been filtered at all, which illustrates that the results in the 2D model case are not a function of the filtration used. The consistent results of the two approaches and the fact that space plasmas are generally quasineutral suggests that the initial direct assumption of quasineutrality might be a better choice. However, the simplicity of the formalism of the zeroth order model is a result of assuming $k_y=0$ and a constant density in the perpendicular direction. The closure in the first order approach is not limited by these assumptions and allows for a simple formulation in terms of the traditional single fluid MHD equations. The aim here has been to contrast the two approaches and better understand what the closure schemes entail. The choice of approach is best decided by the application.

In addition, as both models do not account for ion motion parallel to the field line, they are valid only in the limit of the plasma β on the order of m_e/m_i [which is the case for the parameters used here, $\beta=2\mu_o nkT/B_o^2=\frac{1}{2}(m_e/m_p)$ for $v_{th}=1.41$] where shear Alfvén waves are strongly resonant with electrons. In this range, the results are consistent with the inertial Alfvén wave dispersion relation for $\beta \ll m_e/m_i$ and the kinetic Alfvén wave dispersion relation for $m_e/m_i \ll \beta \ll 1$ (neglecting the ion gyroradius term).[22,26] The Landau damping rates predicted in this range are in agreement with the kinetic dispersion relation derived in Ref. 22. Therefore, the model is valid for both electron inertial and thermal effects in this low β range, but of limited validity as the β gets substantially larger than m_e/m_i and tends toward 1 as the importance of the shear Alfvén wave interaction with ions grows. As the models were designed for study of Alfvén wave effects in the electron acceleration region where the plasma $\beta \ll m_e/m_i$ (Refs. 26 and 27), neglecting the ion effects is justified to first order.

The additional advantage of these hybrid approaches is that by not incorporating kinetic ions, they save on the extensive computational time needed to consider the full ions dynamics thus making it simpler to study large scale systems such as the field line resonance. However, future comparisons with fully kinetic approaches (as used in Ref. 28) (or extending the present models to include kinetic ions) are necessary to more clearly elucidate the limits of the current approximation for the long term evolution of the system. As well, although the present hybrid models do not consider ion kinetic effects, fully kinetic PIC models are sometimes limited by the necessity to choose the ratio of m_i/m_e unrealistically low and thus the contrast of approaches is beneficial for the overall study of the system.

IV. SIMULATIONS WITH DENSITY GRADIENT

For the following section a symmetric density profile as a function of z was designed. This is displayed in Fig. 10 and is given mathematically by

$$n_e = \begin{cases} n_{e_1} & \text{if } z < b \\ \dfrac{n_{e_1} - n_{e_2}}{2} \cos[\pi(z-b)/a] + \dfrac{n_{e_1} - n_{e_2}}{2} + n_{e_2} & \text{if } b < z \leqslant a+b \\ n_{e_2} & \text{if } a+b < z \leqslant L-(a+b) \\ \dfrac{n_{e_1} - n_{e_2}}{2} \cos(\pi[z-[L-(a+b)]]/a - \pi) + \dfrac{n_{e_1} - n_{e_2}}{2} + n_{e_2} & \text{if } L-(a+b) < z \leqslant L-b \\ n_{e_1} & \text{if } L-b < z \leqslant L \end{cases},$$

where n_{e_1} is the electron number density of the well, n_{e_2} is constant high density region at either end of the range in z, b is the length of constant regions of number density n_{e_2}, and a is the length of the sloped regions connecting the areas of constant density. For the 2D model, the density was assumed to be constant in the x direction. The original aim for defining a profile of this nature was to consider the case along the earth's closed field lines where the density is relatively constant along the field line until there is a large increase toward the ionospheric boundaries at either end of the field line. Addressing this in a more complete way though is left to future work.

Since we will be considering large values of k_x, corresponding to small perpendicular scale lengths in x, the term dropped in Eq. (16) must be retained and the expression for the parallel electric field becomes

$$\frac{\partial^2 E_z}{\partial x^2} - \frac{1}{\lambda_e^2} E_z = \frac{\partial}{\partial z}\left(\frac{\partial E_x}{\partial x}\right) + \mu_o e \frac{\partial D_e}{\partial z} - \frac{1}{\epsilon_o}\frac{\partial}{\partial z}\int_0^t dt(\vec{\nabla}\cdot\vec{j}),$$

where as in Ref. 22, E_z is determined using a tridiagonal solver (where a three-point representation was used for $\partial^2 E_z/\partial x^2$) after the calculation of the right-hand side. For comparisons between the 1D and 2D models, the same perturbations as outlined in Sec. II C were used except that the amplitude in Eq. (21) [and correspondingly in Eq. (22)] was halved in order to keep the density fluctuations small.

A. Static parallel electric fields: No Alfvén wave perturbation

Before introducing the perturbation α_o, we examine the static case to see the structure of the parallel electric field generated to support the imposed density gradient. In Fig. 11(a) is displayed the field aligned density profile for the parameters $a=5$, $b=1.5$, $n_{e_1}=0.25$, and $n_{e_2}=1.25$, where the value of n_{e_1} is the same as used for the constant density in the last section. Figure 11(b) displays the parallel electric field profiles from the 1D hybrid model that support the density gradient for two background maxwellian distribution functions with thermal velocities of $v_{\text{th}}=0.71$ and $v_{\text{th}}=1.41$. As expected, fields of opposite sign support the opposing density gradients and a significantly larger field is required in the $v_{\text{th}}=1.41$ case since the energy of the electrons is significantly larger than in the former case. The profiles displayed here are for $t=5$ and although there are minor shorter wavelength fluctuations in profiles over time, they maintain the same basic large scale length profile over the entire length of the run. These simulations (and those in Sec. IV B) used 50 grid points with a time step of 1.25×10^{-3} and 3×10^5 simulation electrons to clearly see the parallel electric field profiles without any postsimulation filtration.

It should be noted that to have a constant temperature profile in the presence of a density gradient is not a necessarily realistic situation, but the aim here is simply to examine the operation of the models in this limit rather than accurately represent a physical system. Generally (and as evident in two fluid simulations), the electrons would try to adjust so that $\vec{\nabla}\cdot\vec{P}=0$ along the field line. These hybrid models, however, do not reproduce this behavior as the MHD component does not account for ion motion parallel to the field line. However, the situation as presented here is not entirely unrealistic and can occur where ions are gravitationally bound (such as in the auroral ionosphere), and static field aligned electric fields exist to support the electron population and maintain quasineutrality. As well, since the response time of ions along the field line is much slower than

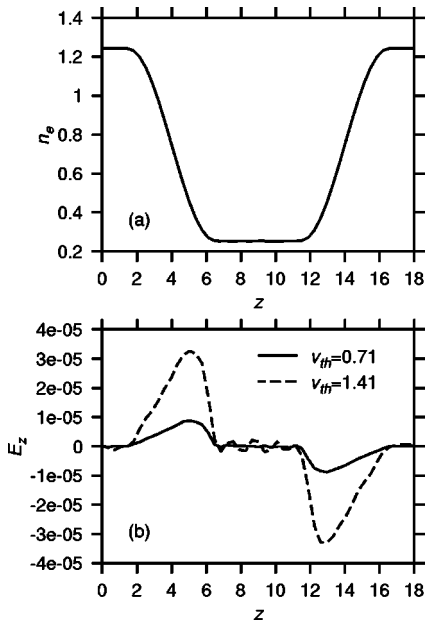

FIG. 11. (a) Density profile constructed with $a=5$, $b=1.5$, $n_{e_1}=0.25$, and $n_{e_2}=1.25$. (b) Static parallel electric field needed to support the density profile for $v_{th}=0.71$ (solid line) and $v_{th}=1.41$ (dashed line) at $t=5$.

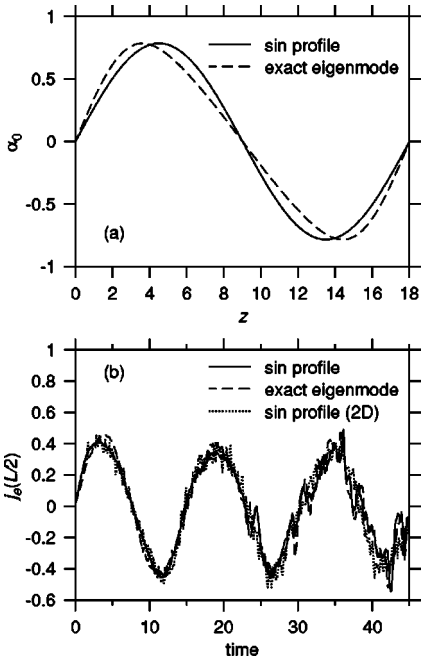

FIG. 12. (a) Exact shear Alfvén wave perturbation eigenmode for α (dashed line) for the density profile in Fig. 11 compared with sinusoidal perturbation (solid line). (b) Field aligned electron current at $L/2$ for runs using the sin perturbation for both the 1D hybrid (solid line) and 2D hybrid (dotted line) models and exact eigenmode perturbation (dashed line) in the 1D model.

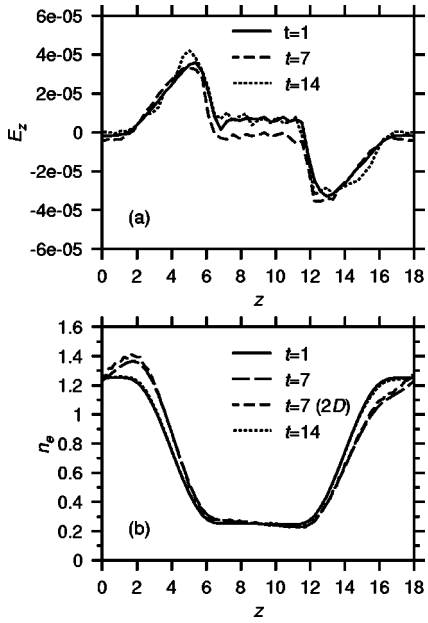

FIG. 13. (a) Fluctuation of the parallel electric field over an Alfvén period for the 1D hybrid model using the sin perturbation in Fig. 12. (b) Corresponding electron number density fluctuations (including 2D hybrid model comparison).

the electrons, the time scale for the evolution toward $\nabla \cdot \vec{P} = 0$ can mean that quasistatic parallel electric fields must persist for long periods relative to the electron transit timescale across the region of density gradient.

B. Electric field and density perturbations

For the constant density case, the sin profile for α_o used was an exact eigenmode of the system, but that is not the case with the variable density profile. This is illustrated in Fig. 12(a) where the exact eigenmode for the density profile used in the simulations with no perturbation is plotted along with a sin profile of the same amplitude. The exact eigenmode was determined from the solution of the dispersion relation using the shooting method. The two profiles do not strongly diverge and so it was not expected that using the exact eigenmode over a sin profile would change the evolution of the system dramatically. This is confirmed in Fig. 12(b) where the parallel current density at $L/2$ is plotted as a function of time for both profiles using the 1D hybrid model and using the sin profile in the 2D model. The results are generally very consistent with each other, although as would be expected the 1D and 2D models using the initial sin perturbation are the closest. This also confirms that both the zeroth and first order closure schemes yield consistent results in the case where field aligned density gradients are present. For the 2D model calculations, 100 grid points were used in each direction with a time step of 2.5×10^{-4} and 10×10^{6} simulation electrons. The electron inertial length λ_e was allowed to vary as a function on n_e as it resulted in greater numerical stability in the presence of the steep density gradients under consideration here.

Figure 13 illustrates the parallel electric field and density perturbations at three times over the first Alfvén period using the 1D hybrid model with the sin perturbation. Comparison of Figs. 13(a) and 11(b) illustrates that the gross profile of the parallel electric field is the same as the static profile with the same temperature. Therefore, the picture that emerges is that there is time dependent parallel electric field contribution from the shear Alfvén wave perturbation that sits on top of the static field. The corresponding electron number density fluctuations are illustrated in Fig. 13(b) and parallel electric field profiles are generally most consistent at the beginning and end of the period when the density profile has returned more or less to its initial state. Of course, if the density fluctuations are too large as would happen if the amplitude of the α_o perturbation were very strong or k_x were large, this simple picture would break down and the perturbations of the parallel electric field could dominate over the static profile. Also illustrated in Fig. 13(b) is the electron number density profile from the 2D model at $t=7$ which is very close to the 1D result at the same time further illustrating the consistency of the two approaches.

C. Landau damping

The aim of this section is to investigate how Landau damping is affected by the presence of a field aligned density gradient. This was accomplished by doing a series of runs starting with constant electron number density n_{e_1} and then gradually filling in the well until the second constant density system $2n_{e_1}$ was reached. This progression is illustrated in Fig. 14. The wells in this case are not as deep as in the previous examples in this section because the damping rate

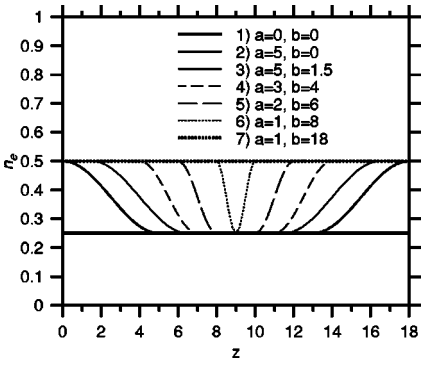

FIG. 14. Density profiles used in Landau damping study.

for $n_e=1.25$ was too low. As is, the system progresses between two constant densities, both of which are relatively heavily damped.

In all cases, the system was perturbed by the same sin profile for α_o. As with the calculations in Sec. IV B, the amplitude of the shear velocity in Eq. (21) was halved, but the value of k_x was doubled ($k_x=2\pi/0.1$) and so the amplitude for α_o was double that in Fig. 12(a). The value of k_x was increased to make the damping visible in a few Alfvén periods and the values of u_{y0} were kept small so that the perturbation density fluctuations would not completely dominate the background profile. For these calculations, the number of grid points was increased to 100 due to the steepness of some of the profiles, the time step was dropped to 6.6×10^{-4} and 1×10^5 simulation electrons were used.

The evolution of the parallel current density at $L/2$ in each case is illustrated in Fig 15. As is evident, the damping

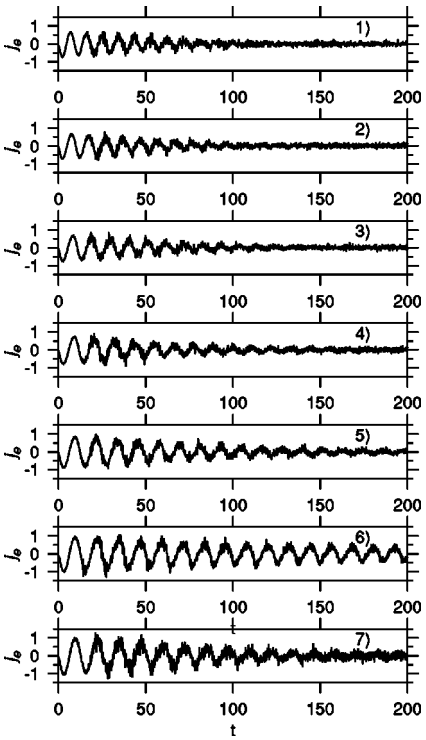

FIG. 15. Parallel current density at $z=L/2$ as a function of time for the density profiles illustrated in Fig. 14.

TABLE I. Computed periods, frequencies, and damping rates from Fig. 15.

Case	Period	Frequency (ω)	Damping rate (γ)	γ/ω
1	9.1	0.690	-0.017 ± 0.002	-0.025
2	9.9	0.634	-0.018 ± 0.002	-0.028
3	10.8	0.581	-0.017 ± 0.002	-0.029
4	11.8	0.532	-0.016 ± 0.002	-0.030
5	12.3	0.511	-0.011 ± 0.002	-0.022
6	12.6	0.498	-0.006 ± 0.002	-0.011
7	12.8	0.490	-0.010 ± 0.002	-0.020

rate slowly decreases as the well is filled, migrating from the first constant density limit to the second. This is as would be expected with the one extra interesting feature of almost no damping in case 6 which corresponds to the situation of a narrow well. Somehow, the adjacent presence of static fields supporting the opposing density gradient makes less efficient the wave-particle interactions upon which the damping depends. It should be noted that when an additional simulation was done with the well centered at about $z=15$, this feature vanished and the system was damped consistent with the others. Therefore, the relative phase between the well and wave is important for electron phase space orbits to be effected in the "correct" way to impede the damping. A more detailed analysis of what is occurring in this case is beyond the scope of this work and so will be left for future studies.

These qualitative results are emphasized in Table I where the period, frequency and damping rate γ are tabulated. The damping rates were computed from the natural log of the absolute values of the period and half period points in Fig. 15. The profiles were first filtered to clear off the high frequency noise and only points for $t\leqslant70$ were used in the calculation. As is evident, the damping rate for case 6, is smaller by at least of a factor of 2 from all the others. This is also the case in the last column of the table for γ/ω. This ratio more or less represents the damping efficiency per Alfvén cycle which given the range of error seems relatively constant except for the significant drop for case 6.

The damping rates for the two constant density cases was determined from the dispersion relation of the hybrid MHD-kinetic system (see Ref. 22). For $n_{e_1}=0.25$ and $n_{e_2}=0.5$ the theoretical damping rates were -0.0157 and -0.00989 respectively which are in good agreement with the numerical rates in Table I for cases 1 and 7.

Although not displayed here, a series of runs was tried where "*a*" (the range of the gradient region) was set to 1 and "*b*" was adjusted to fill in the well. The same qualitative behavior was evident as noted here. Therefore, the ratio of the areas covered by each density region is probably more significant to the damping behavior than the steepness of the gradients (with the exception of case 6).

V. SUMMARY AND DISCUSSION

We have contrasted two methods of closure for hybrid MHD-kinetic models of shear Alfvén waves in constant and variable density systems and developed the energy invariant in one and two dimensions. The first method used in Ref. 21

directly assumed quasineutrality in the form $\nabla \cdot \vec{j}=0$ while the second method used in Ref. 22 allowed for a nonzero divergence in the current density which in-turn produced a "correcting" electric field. In both cases, the parallel electric field was obtained from a version of the generalized Ohm's law.

It was found that both models yielded equivalent results as long as the full generalized Ohm's law was used when quasineutrality was assumed. Otherwise, the method used in Ref. 21 strongly diverged from both the other hybrid model results and that of the cold plasma MHD illustrating that the pressure term is of significant importance. The model used in Ref. 22, on the other hand, yielded similar results whether or not the pressure term was included.

The reason for the difference is that in the second method, the generalized Ohm's law can be viewed as a good first guess to what the parallel electric field should be and if the guess is not sufficiently good, the plasma is not as quasineutral as it would like to be and consequently generates a compensating electric field. The end result being that quasineutrality is a consequence of the system rather than being an initial assumption.

Therefore, both methods are useful for the study of standing shear Alfvén waves in magnetospheric plasmas, but it should be clearly understood that in the method used in Ref. 22 disconnecting terms alone in the generalized Ohm's law does not elucidate the importance of that term to the determination of E_z as it will be compensated for by the closure scheme. The method does have the advantage though of incorporating the full set of cold plasma MHD equations (which could be further generalized) as well as easily allowing for density gradients in either the perpendicular or parallel directions.

In the case of field aligned density profiles, the models were illustrated to produce a static parallel electric field when there was no shear Alfvén wave perturbation. The magnitude of the field increased with plasma temperature. When the perturbation was applied, the parallel electric field more or less oscillated around an average value that was very similar to the static profile.

In addition, a series of runs were done to study Landau damping in the presence of a density gradient. It was illustrated, that the Landau damping was not hindered by the presence of the density gradient except in the case of a narrow central well.

In this paper we have concentrated on the case of a uniform magnetic field but, as mentioned earlier, converging magnetic field and mirror force effects are crucial to a more complete understanding of the electron response in the auroral acceleration region. To address this, investigations are currently under way using a version of the first order model in dipolar coordinates (developed in Ref. 29).

ACKNOWLEDGMENTS

P.A.D. is funded by a PPARC grant. Simulations were conducted using both the SRIF and PPARC funded St. Andrews Maths Cluster and the WESTGRID computing facilities at the University of Alberta funded by the Canadian Foundation for Innovation (CFI) and the Province of Alberta. R.D.S. acknowledges support from the Gradviertenkolleg in Hochtemperatur-Plasmaphysik at the Univ. of Duesseldorf, Germany.

APPENDIX: HYBRID MODEL ENERGY INVARIANT

The standard approach for the derivation of an energy invariant for a system is to put the equations in the conservation form

$$\frac{dW}{dt} + \nabla \cdot \vec{S} = 0, \tag{A1}$$

where W represents the total energy and $\vec{S}$ is the energy flux. For the system of MHD equations and kinetic electrons, this takes the form

$$\frac{d}{dt}\int \left(\frac{1}{2}\rho_o u^2 + \frac{b^2}{2\mu_o}\right) dV + \frac{d}{dt}\sum_i \frac{1}{2} m_e v_i^2 + \int \left(\frac{\vec{E}\times\vec{b}}{\mu_o}\right)\cdot d\vec{s} = 0. \tag{A2}$$

Since $\vec{E}$ and $\vec{b}$ are periodic in z, the net Poynting flux across the boundaries cancels and so after integrating with respect to time, the invariant becomes

$$\int_V \left(\frac{1}{2}\rho_o u^2 + \frac{b^2}{2\mu_o}\right) dV + \sum_i \frac{1}{2} m_e v_i^2 = T_E, \tag{A3}$$

where T_E is the total energy and is constant in time. Now, as each of the simulation electrons are "superparticles" representative of a large number of electrons, the term of the electron kinetic energy must be appropriately scaled such that

$$T_E = \int_V \left(\frac{1}{2}\rho_o u^2 + \frac{b^2}{2\mu_o}\right) dV + \frac{N}{N_p}\frac{1}{2} m_e \sum_i v_i^2, \tag{A4}$$

where $N=\int n_e dV$ is the total number of real electrons represented in the simulation volume, n is the electron number density, and N_p is the total number of simulation electrons.

Since the model is 2D and $k_y=0$, a constant y dependence is assumed for each variable and factored out as a length scale so that in nondimensional form the expression represents the energy per unit y,

$$T_{E_{2D}} = \frac{T_E}{\Delta y} = \int_A dxdz \frac{\rho_o u_y^2}{2} + \int_A dxdz \frac{b_y^2}{2} + \frac{1}{2} C_{e2} \sum_i v_i^2, \tag{A5}$$

where $C_{e2}=(m_e/m_p)(\int n_e dxdz/N_p)$ is a constant and the fact that $u_x=b_x=b_z=0$ has been used as well.

For the 1D system, the volume of integration in Eq. (A2) has dimensions Δy in y, L_z in z, and extent Δx (tending to 0) in x. This yields an expression for energy conservation in the form

$$T_{E_{1D}} = \frac{T_E}{\Delta x \Delta y} = \int_0^{L_z} \left(\frac{1}{2}\rho_o u_y^2 + \frac{b_y^2}{2\mu_o} \right) dz + \frac{\int n_e dz}{N_p} \sum_i \frac{1}{2} m_e v_i^2 + \frac{1}{\mu_o} \int_0^t dt [E_x(L_z) b_y(L_z) - E_x(0) b_y(0)] - \frac{1}{\mu_o} \int_0^t \int_0^{L_z} \frac{\partial (E_z b_y)}{\partial x} dz dt,$$

where the last two terms are from the integral of the Poynting flux around a box of width Δx and length L_z centered on the magnetic field line.

Expanding the derivative in the last term and then using Ampère's law ($\partial b_y / \partial x = \mu_o j_z$) this becomes

$$T_{E_{1D}} = \frac{T_E}{\Delta x \Delta y} = \int_0^{L_z} \left(\frac{1}{2}\rho_o u_y^2 + \frac{b_y^2}{2\mu_o} \right) dz + \frac{\int n_e dz}{N_p} \sum_i \frac{1}{2} m_e v_i^2 + \frac{1}{\mu_o} \int_0^t dt [E_x(L_z) b_y(L_z) - E_x(0) b_y(0)] - \frac{1}{\mu_o} \int_0^t \int_0^{L_z} \left(b_y \frac{\partial E_z}{\partial x} + \mu_o E_z j_e \right) dz dt,$$

where $j_z = j_e$ has been used. The magnetic field line can always be considered to be a nodal point so that $u_y = b_y = 0$ and so the total energy invariant is just a balance between the perpendicular Poynting flux and the kinetic energy of the electrons. With the scaling discussed previously, this is expressed in nondimensional form as

$$T_{E_{1D}} = \frac{T_E}{\Delta x \Delta y} = -\int_0^t \int_0^{L_z} (E_z j_e) dz dt + \frac{1}{2} C_{e1} \sum_i v_i^2, \quad \text{(A6)}$$

where $C_{e1} = (m_e / m_p) \int n_e dz / N_p$.

[1] C. Wei, J. Samson, R. Rankin, and P. Prycz, J. Geophys. Res. **99**, 11 (1994); **99**, 265 (1994).
[2] A. N. Wright, W. Allan, M. S. Ruderman, and R. Elphic, J. Geophys. Res. **107**, 1120 (2002).
[3] R. Rankin, J. Samson, and V. Tikhonchuk, Geophys. Res. Lett. **26**, 3601 (1999).
[4] K. Ronnmark, J. Geophys. Res. **107**, 1430 (2002).
[5] R. Chodura, Nucl. Fusion **15**, 55 (1975).
[6] A. Sgro and C. Nielson, Phys. Fluids **19**, 126 (1976).
[7] S. Hamsaki, N. Krall, C. Wagner, and R. Byrne, Phys. Fluids **20**, 65 (1977).
[8] D. Hewett, J. Comput. Phys. **38**, 378 (1980).
[9] M. Leroy, C. Goodrich, D. Winske, C. Wu, and K. Papadopoulos, Geophys. Res. Lett. **8**, 1269 (1981).
[10] S. Brecht and V. Thomas, Comput. Phys. Commun. **48**, 135 (1988).
[11] D. Swift, Geophys. Res. Lett. **22**, 311 (1995).
[12] D. Winske and N. Omidi, J. Geophys. Res. **101**, 17287 (1996).
[13] M. Hesse and D. Winske, Geophys. Res. Lett. **20**, 1207 (1993).
[14] D. Winske and K. Quest, J. Geophys. Res. **91**, 8789 (1986).
[15] P. Lyster and J.-N. Leboeuf, J. Comput. Phys. **102**, 180 (1992).
[16] B. Thompson and R. Lysak, J. Geophys. Res. **101**, 5359 (1996).
[17] C. Chaston, C. Carlson, R. Ergun, and J. McFadden, Phys. Scr., T **T84**, 64 (2000).
[18] C. Chaston, J. Bonnell, L. Peticolas, C. Carlson, J. McFadden, and R. Ergun, Geophys. Res. Lett. **29**, 1535 (2002).
[19] C. Chaston, J. Bonnell, C. Carlson, J. McFadden, R. Ergun, and R. Strangeway, J. Geophys. Res. **108**, 8003 (2003).
[20] C. Watt, R. Rankin, and R. Marchand, Phys. Plasmas **11**, 1277 (2004).
[21] C.-H. Hui and C. Seyler, J. Geophys. Res. **97**, 3953 (1992).
[22] P. A. Damiano, R. Sydora, and J. Samson, J. Plasma Phys. **69**, 277 (2003).
[23] V. Tikhonchuk and R. Rankin, Phys. Plasmas **7**, 2630 (2000).
[24] A. N. Wright and A. Hood, J. Geophys. Res. **108**, 1135 (2003).
[25] C. Birdsall and A. Langdon, *Plasma Physics Via Computer Simulation* (Adam Hilger, Bristol, U. K., 1991).
[26] R. L. Lysak and W. Lotko, J. Geophys. Res. **101**, 5085 (1996).
[27] C. Goertz and R. Boswell, J. Geophys. Res. **84**, 7239 (1979).
[28] F. Tsung, G. Morales, and J. Leboeuf, Phys. Rev. Lett. **90**, 055004 (2004).
[29] P. Damiano, Ph.D. thesis, University of Alberta, 2002.